Volume 25
Number 25
7 July 2023
Pages 3581–3704

CrystEngComm

rsc.li/crystengcomm

ISSN 1466-8033

ROYAL SOCIETY OF CHEMISTRY

COMMUNICATION

Pradip Chakraborty, Francisco Javier Valverde-Muñoz, Eric Collet *et al.*

Ferroelastic phase transition and the role of volume strain in the structural trapping of a metastable quenched low-spin high-symmetry phase in $[Ru_{0.35}Fe_{0.65}(ptz)_6](BF_4)_2$

CrystEngComm

COMMUNICATION

View Article Online
View Journal | View Issue

Cite this: *CrystEngComm*, 2023, **25**, 3588

Received 14th April 2023,
Accepted 20th May 2023

DOI: 10.1039/d3ce00365e

rsc.li/crystengcomm

Ferroelastic phase transition and the role of volume strain in the structural trapping of a metastable quenched low-spin high-symmetry phase in $[Ru_{0.35}Fe_{0.65}(ptz)_6](BF_4)_2$†

Francisco Javier Valverde-Muñoz, *[a] Ricardo Guillermo Torres Ramírez, [a] Abhilash Ulhe, [a] Elzbieta Trzop, [ab] Mousumi Dutta,[c] Chinmoy Das,[c] Pradip Chakraborty*[c] and Eric Collet *[abd]

Spin-crossover (SCO) materials exhibit thermal conversion of their electronic state from low (LS) to high (HS) spin state, which also involves both intra- and inter-molecular structural reorganisations within the crystal. The occurrence of coupled SCO and symmetry-breaking (SB), also responsible for structural reorganisations, is a current topic of interest because it can generate exotic behaviours such as unsymmetric hysteresis loops, stepwise evolution of the spin conversion, or sequences of phase transitions. Here we study the coupling and decoupling of SCO and SB during the thermal conversion of the prototypical $[Fe(ptz)_6](BF_4)_2$ compound diluted in the isostructural ruthenium host lattice $[Ru(ptz)_6](BF_4)_2$. We show that the $[Ru_{0.35}Fe_{0.65}(ptz)_6](BF_4)_2$ system undergoes a SB between the high-spin high symmetry (HShs) phase ($R\bar{3}$ space group) and the low-spin low symmetry (LSls) phase ($P\bar{1}$ space group). We present a structural analysis of the ferroelastic $R\bar{3} \rightarrow P\bar{1}$ phase transition and highlight the structural SB signatures. We also study the metastable low-spin high symmetry (LShs) phase ($R\bar{3}$ space group) reached upon fast cooling. In the framework of the Landau theory of phase transition adapted by Collet, and considering the elastic coupling between SCO and SB, we discuss the structural distortion between the HShs, LShs, and LSls phases and explain the metastable nature of the LShs phase.

Introduction

Entropy-driven molecular bistability, between electronic states separated by an energy barrier of the order of thermal energy, can give rise to crossover phenomena at thermal equilibrium between different electronic states, including charge-transfer or spin states, for example.[1] In molecular materials, elastic interactions between sites, for which the change of electronic state is associated with the volume change, can induce cooperative phase transitions associated with thermal hysteresis.[2] In many cases, this phenomenon occurs without symmetry change. In solids, symmetry-breaking (SB) phase transitions can also occur, and more and more systems exhibit concerted or sequential changes in electronic state and symmetry.[2b,3] This is the case of the spin-crossover (SCO) compound $[Fe(ptz)_6](BF_4)_2$ iron(II) (ptz = 1-propyltetrazole), which exhibits a spin-transition hysteresis at atmospheric pressure.[4] The thermal dependence of the fraction γ of high-spin molecules changes discontinuously through a ≃7 K wide thermal hysteresis. This change of electronic state results from the rearrangement of electrons within metal d-orbitals between the high-spin (HS, $S = 2$) and low-spin (LS, $S = 0$) configurations. The high-temperature HS phase is the high symmetry one (HShs), with a rhombohedral $R\bar{3}$ space group, while the low-temperature LS phase is low symmetry (LSls) with a triclinic $P\bar{1}$ space group.[4a,d,g,h,5] There are different contributions to the entropy increase between the LSls and HShs phases. On the one hand, the non-symmetry-breaking SCO includes an electronic entropy change due to the change in spin multiplicity and a vibrational entropy due to the global decrease of the frequency of the modes between LS and HS states.[1h,2g,6] On the other hand, there is also a SB contribution due to the order–disorder configurational change and splitting of mode frequencies, and therefore, SCO and SB can occur simultaneously or sequentially depending

[a] *Univ Rennes, CNRS, IPR (Institut de Physique de Rennes) – UMR 6251, 35000 Rennes, France. E-mail: francisco-javier.valverde-munoz@univ-rennes.fr, eric.collet@univ-rennes.fr*
[b] *Department of Chemistry, DYNACOM IRL2015 University of Tokyo – CNRS – UR1, 7-3-1 Hongo, Tokyo 113-0033, Japan*
[c] *Department of Chemistry, Indian Institute of Technology Kharagpur, Kharagpur-721302, India. E-mail: pradipc@chem.iitkgp.ac.in*
[d] *Institut universitaire de France (IUF), France*

† CCDC 2256112–2256114. For crystallographic data in CIF or other electronic format see DOI: https://doi.org/10.1039/d3ce00365e

upon the external parameters.[2a,3b] Indeed, under pressure, the $[Fe(ptz)_6](BF_4)_2$ system exhibits sequential conversions on cooling with SB from the HShs phase towards a high-spin low symmetry (HSls) $P\bar{1}$ phase, followed SCO towards the low-spin low symmetry (LSls) $P\bar{1}$ phase.[4c,e] In addition, upon fast cooling, a metastable low-spin high-symmetry (LShs) $R\bar{3}$ phase appears.[7]

It was recently shown that the dilution of the $[Fe(ptz)_6](BF_4)_2$ compound in the isostructural Ru host lattice $[Ru(ptz)_6](BF_4)_2$, which also undergoes the same $R\bar{3} \rightarrow P\bar{1}$ crystallographic phase transition upon cooling, stabilises the Fe(II) low-spin state.[7d] In the $[Ru_{0.35}Fe_{0.65}(ptz)_6](BF_4)_2$ system (**1**) studied here, the half conversion temperature was found to be of the order of 135 K, *i.e.*, ≃8 K above the one of the neat $[Fe(ptz)_6](BF_4)_2$ compound. This results from the fact that the Ru(II) host, with lattice dimensions similar to the lattice of the pure LS Fe(II) compound, induces a chemical pressure favouring LS Fe(II) complex of lower volume, shifting SCO towards higher temperatures compared to pure $[Fe(ptz)_6](BF_4)_2$. In the previous structural characterisation of (**1**) performed by single-crystal X-ray diffraction, three different phases were identified.[7d] Above 150 K, the HShs phase is exclusively dominant, displaying the $R\bar{3}$ space group. At 150 K, the lattice parameters of the hexagonal lattice are: $a_H = b_H = 10.83$ Å, $c_H = 32.03$ Å. Below ≃130 K two possible low-spin phases can be generated, depending on the cooling rate of crystals. On the one hand, a slow cooling (≃0.2 K min^{-1}) induces a LSls phase, which has a triclinic lattice ($P\bar{1}$ space group) with $a_P = 12.33$ Å, $b_P = 10.77$ Å, $c_P = 16.37$ Å, $\alpha = 90.20°$, $\beta = 100.54°$ and $\gamma = 90.20°$. On the other hand, fast quenching at 80 K from the HShs phase induces low-temperature LShs phase, which retains the $R\bar{3}$ space group, with lattice parameters $a_H = b_H = 10.73$ Å, $c_H = 32.01$ Å. Therefore, SB and SCO may decouple in the $[Ru_{0.35}Fe_{0.65}(ptz)_6](BF_4)_2$ solid solution.

In the framework of the Landau theory adapted by Collet for coupled SB and SCO,[2a,3a–c] the theoretical phase diagram of $[Fe(ptz)_6](BF_4)_2$ was described through the evolution and coupling of SCO and SB phenomena with temperature and pressure. It provided an excellent qualitative agreement with the experimental data through the evolution of SCO curves or lattice deformations under pressure.[2a] In the present paper, we study the evolution of SCO and SB during the thermal conversion of (**1**). First, we present a detailed structural analysis of the HShs-to-LSls phase transition and highlight the associated symmetry-breaking signatures in both real and reciprocal spaces. These show that structural phase transition corresponds to a ferroelastic $R\bar{3} \rightarrow P\bar{1}$ symmetry-breaking phase transition, with a group-subgroup relationship, and not to a reconstructive phase transition. In such a case, the Landau theory approach is relevant to describe the observed phenomena. We also study the metastable low-spin high symmetry (LShs) phase ($R\bar{3}$ space group) reached upon fast cooling. Within the Landau theory framework of phase transition adapted by Collet, we explain that the metastable nature of the LShs phase is due to the partial volume strain, containing only the contribution of the SCO and not the SB one.

Results and discussion

Materials and methods

Mixed crystals of $[Ru_{0.35}Fe_{0.65}(ptz)_6](BF_4)_2$ were synthesised from previously synthesised $[Ru(ptz)_6](BF_4)_2$ and $[Fe(ptz)_6](BF_4)_2$ crystals, separately redissolved in CH_3CN. The two solutions were mixed homogeneously to obtain $[Ru_{0.35}Fe_{0.65}(ptz)_6](BF_4)_2$ single crystals. Details of the synthesis and characterisation were reported by Chakraborty *et al.*[7d]

Single-crystal X-ray diffraction (SCXRD) data of the complex (**1**) were collected on the same single crystal at 250 K (HShs) and 80 K (LSls) on slow cooling (≃0.2 K min^{-1}) as well as on flash cooling at 80 K (LShs) using an Oxford Diffraction Xcalibur3 X-ray diffractometer with an enhanced source, using Mo K_α (λ = 0.71073 Å) radiation, fitted with a Sapphire3 detector. Changes in unit cell volume, cell parameters, and Bragg peak intensities as a function of temperature were investigated on a new single crystal during cooling from 250 K to 80 K and warming from 80 to 250 K (2–3 K steps with 200 K h^{-1} cooling/heating rate). Single crystals were mounted on cryo-loops with Parabar 10312 oil. Nitrogen flow 700Plus series cryostat from Oxford Cryosystems was used for the variable-temperature measurements and the complete data collections. The CrysAlisPRO95 software package from Rigaku Oxford Diffraction was used for all data collections and data processing (indexing, integration, and reduction). All structures were solved by dual direct methods with SHELXT[8] and refined by full-matrix least-squares on F^2 using SHELXL[9] in OLEX2.[10] All non-hydrogen atoms were refined anisotropically and H-atoms were constrained by geometry. When applicable, DFIX, SIMU and ISOR restraints as well EADP and EXYZ constraints were applied for occupational disorders of selected atoms sites. In case of 80 K data in LSls phase, a domain formation upon transition was detected; only data of a main domain component were taken for final structure determination here. CCDC 2256112 (250 K), CCDC 2256113 (80 K flash cooling), and CCDC 2256114 (80 K) contain the crystal data collection and refinement parameter details for this paper.

Group-subgroup symmetry breaking. Fig. 1 shows the nodes of the $R\bar{3}$ rhombohedral lattice and the different unit cells that can be used to describe lattice periodicity: the primitive rhombohedral cell, the hexagonal cell, and the triclinic primitive cell. Any lattice translation vector $\vec{T}$, connecting nodes of the high-temperature lattices can be given in the primitive triclinic $P\bar{1}$ or hexagonal $R\bar{3}$ lattices:

$$\vec{T} = U\vec{a_P} + V\vec{b_P} + W\vec{c_P} = u\vec{a_H} + v\vec{b_H} + w\vec{c_H} \quad (1)$$

where U, V, W, u, v and w are integers. The transformation matrix given in ref. 11 connecting the lattices is:

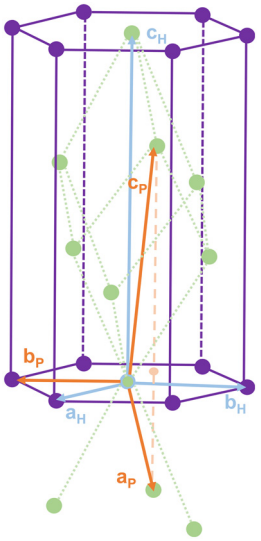

Fig. 1 Nodes of the $R\bar{3}$ rhombohedral lattice (green), showing the relationship with the hexagonal (H subscript purple) and primitive triclinic (P subscript orange) unit cells.

$$\begin{pmatrix} \overrightarrow{a_P} \\ \overrightarrow{b_P} \\ \overrightarrow{c_P} \end{pmatrix} = \begin{pmatrix} -\frac{2}{3} & -\frac{1}{3} & -\frac{1}{3} \\ 0 & -1 & 0 \\ -\frac{2}{3} & -\frac{1}{3} & \frac{2}{3} \end{pmatrix} \begin{pmatrix} \overrightarrow{a_H} \\ \overrightarrow{b_H} \\ \overrightarrow{c_H} \end{pmatrix} \quad (2)$$

consequently, any vector $\vec{Q}$ of the reciprocal space can be expressed both in the $P\bar{1}$ triclinic reciprocal cell or in the $R\bar{3}$ hexagonal reciprocal one:

$$\overrightarrow{Q} = H\overrightarrow{a_P^*} + K\overrightarrow{b_P^*} + L\overrightarrow{c_P^*} = h\overrightarrow{a_H^*} + k\overrightarrow{b_H^*} + l\overrightarrow{c_H^*} \quad (3)$$

Considering the transformation matrix:

$$\begin{pmatrix} \overrightarrow{a_P^*} \\ \overrightarrow{b_P^*} \\ \overrightarrow{c_P^*} \end{pmatrix} = \begin{pmatrix} -1 & 0 & -1 \\ \frac{1}{2} & -1 & 0 \\ -\frac{1}{2} & 0 & 1 \end{pmatrix} \begin{pmatrix} \overrightarrow{a_H^*} \\ \overrightarrow{b_H^*} \\ \overrightarrow{c_H^*} \end{pmatrix} \quad (4)$$

we obtain the following developments:

$$\begin{aligned} &\overrightarrow{Q} = H\overrightarrow{a_P^*} + K\overrightarrow{b_P^*} + L\overrightarrow{c_P^*} \text{ or} \\ &\overrightarrow{Q} = H\left(-\overrightarrow{a_H^*} - \overrightarrow{c_H^*}\right) + K\left(\frac{1}{2}\overrightarrow{a_H^*} - \overrightarrow{b_H^*}\right) + L\left(-\frac{1}{2}\overrightarrow{a_H^*} + \overrightarrow{c_H^*}\right) \end{aligned} \quad (5)$$

and the relationships between the indexes of the $R\bar{3}$ and $P\bar{1}$ reciprocal lattices:

$$h = -H + \frac{1}{2}K - \frac{1}{2}L, k = -K \text{ and } l = -H + L \quad (6)$$

In the conventional $R\bar{3}$ hexagonal lattice cell, only (hkl) peaks with $-h + k + l = 3n$ are present, while (HKL) Bragg peaks are allowed for any H, K, L integers in the primitive triclinic cell. Therefore, in the case of a group-subgroup SB phase transition due to a distortion from hexagonal to triclinic lattices, with a pseudo hexagonal reciprocal lattice, the $R\bar{3} \rightarrow P\bar{1}$ symmetry breaking is characterized by the appearance of Bragg peaks with $-h + k + l \neq 3n$ and also with $h = n + \frac{1}{2}$.

Fig. 2 shows the diffracted intensity in the reciprocal space using the (pseudo) hexagonal cell. The diffraction patterns were obtained from single crystal diffraction data collected at 250 K for the HShs phase and at 80 K for the LSls and LShs phases. We were cautious about the cooling rate when the low-spin phases were generated: the LShs was reached by fast cooling of the single crystals, directly put under the N_2 stream of the cryostat set to 80 K, while the LSls phase was reached on slow cooling ($\simeq$0.2 K min^{-1}) from the HShs phase. The diffraction patterns of the HShs and LShs phases are similar (within the thermal contraction): both exhibit hexagonal reciprocal lattices of $R\bar{3}$ space group with $a_H^* = b_H^*$ and $\gamma_H^* = 60°$, and the Bragg peaks present in the $(hk0)$ or $(h0l)$ reciprocal planes obey $-h + k + l = 3n$. In the LSls phase, the symmetry is broken, as characterized by the appearance of new Bragg peaks on the nodes of the hexagonal lattice and indexed $-h + k + l \neq 3n$ and additional peaks at $h = n + \frac{1}{2}$, in both $(hk0)$ and $(h0l)$ reciprocal planes. As explained above, the presence of these new diffraction peaks at these specific coordinates of the reciprocal space is a direct proof of the symmetry-breaking relationship between the $R\bar{3}$ and the $P\bar{1}$ crystalline structures of (**1**). These results show that the HShs $R\bar{3} \rightarrow$ LSls $P\bar{1}$ phase transition is associated with the loss of the 3-fold symmetry axis along $\overrightarrow{c_H}$, which corresponds therefore to a symmetry-breaking ferroelastic distortion with a group–subgroup relationship.[12] Noteworthy, the metastability of the trapped LShs state is characterized by its relaxation towards the LSls ground state. The associated structural reorganization is characterized by the changes in the X-ray diffraction signal due to the $R\bar{3} \rightarrow P\bar{1}$ ferroelastic distortion discussed above. Even after 17 h, we didn't observe any signature of relaxation of the LShs state thermally quenched at 80 K, which is consistent with previous measurements on the $[Fe(ptz)_6](BF_4)_2$ complex at 90 K.[4a]

Ferroelastic lattice distortions in the LSls phase. The thermal evolutions of the lattice parameters of (**1**), given in the (pseudo) hexagonal cell, were monitored in the 80–250 K range in cooling and warming modes. Fig. 3 show the characteristic $R\bar{3} \rightarrow P\bar{1}$ ferroelastic distortions. In the hexagonal cell of the HShs phase, $a_H = b_H$, $\alpha = \beta = 90°$ and $\gamma = 120°$. In the slow cooling mode, these relationships remain valid down to 136 K. At lower temperatures, we observe a splitting of the lattice parameters a_H and b_H, accompanied by a significant deviation of the lattice angles α and β from 90°. Fig. 2c also shows the distortions of the reciprocal lattice in the LSls phase at 80 K ($\beta^* \neq 90°$, $\gamma^* \neq 60°$). The data in the warming mode show that the $R\bar{3}$ HShs state is restored above 144 K. These curves obtained by single-crystal X-ray diffraction reveal $\simeq$8 K wide thermal hysteresis between the HShs phase and the LSls phase reached on slow cooling.

The thermal dependence of the amplitude of the symmetry-breaking order parameter $\eta(T)$ can be monitored

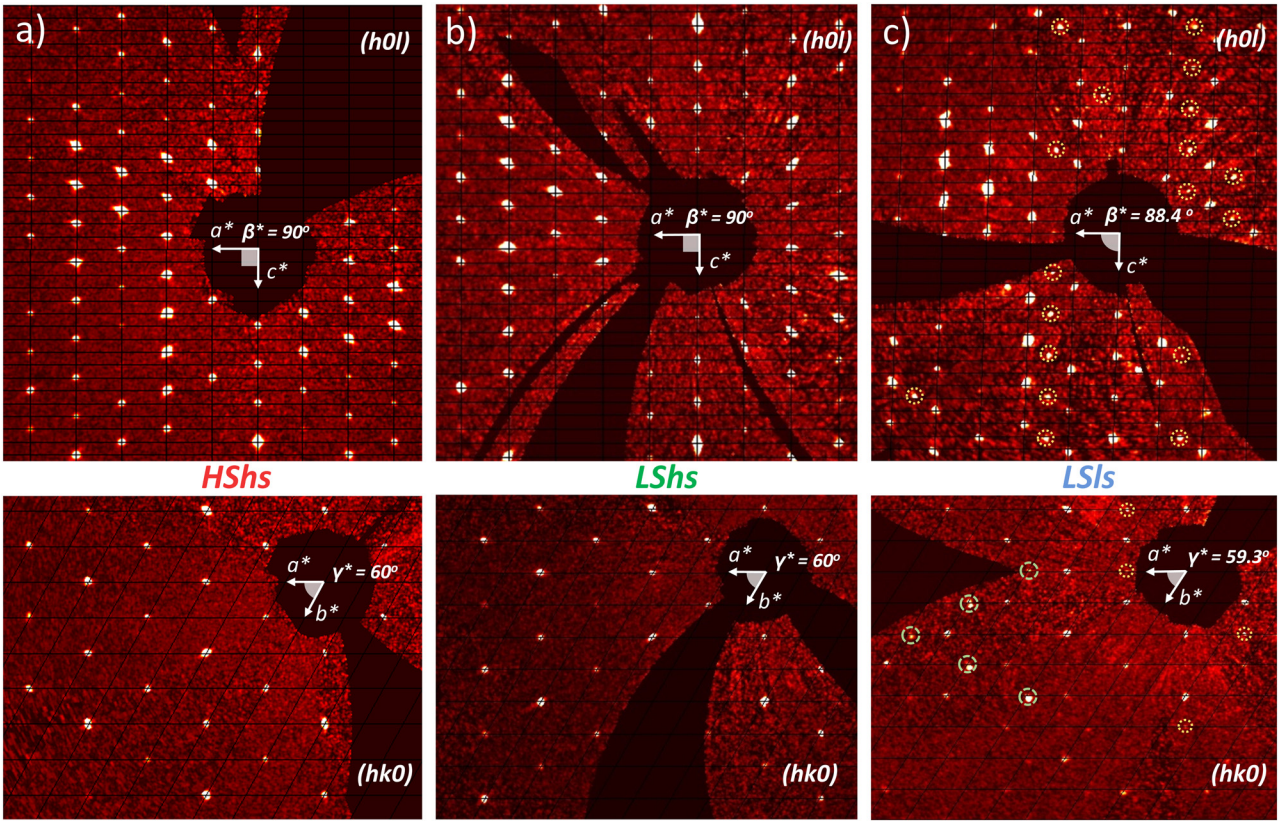

Fig. 2 Diffracted intensity on the nodes of the hexagonal high symmetry reciprocal lattice, for the HShs (a), LShs (b) and LSls (c) phases, in the (*h0l*) plane (top) and (*hk0*) plane (bottom). In the $R\bar{3}$ HShs and LShs phases, only Bragg peaks fulfilling $-h + k + l = 3n$ rule are present. In the LSls phase, Bragg peaks appear at $h = n + 1/2$ and $-h + k + l \neq 3n$.

through the evolution of ferroelastic $R\bar{3} \rightarrow P\bar{1}$ distortions, as shown in Fig. 4a through the evolution of the parameter δ defined as:

$$\delta = \frac{1}{3}(|a_H - b_H|/0.015 + |\alpha - 90°|/0.28 + |\beta - 90°|/0.78) \quad (7)$$

and obtained through a linear fit of the data from Fig. 3. The symmetry change is also characterised by the thermal dependence of the intensity of the symmetry-breaking (*hkl*) Bragg peaks with $-h + k + l \neq 3n$ or $h = n + \frac{1}{2}$ appearing in the LSls phase (Fig. 4a). Both the ferroelastic lattice distortion (δ) and the intensity of the symmetry-breaking Bragg peaks are direct signatures of the $R\bar{3} \rightarrow P\bar{1}$ ferroelastic phase transition. The curves exhibit thermal hysteresis, and the discontinuous symmetry-breaking corresponds to what is expected for the $R\bar{3} \rightarrow P\bar{1}$ ferroelastic phase transition.

Indeed, the symmetry-breaking order parameter η belongs to the bi-dimensional E_g representation of the $\bar{3}$ point group, which restricts the phase transition to first-order.[3c,12d]

For the ferroelastic $R\bar{3} \rightarrow P\bar{1}$ symmetry breaking, three ferroelastic domains form, due to the loss of the 3-fold axis. This translates into X-ray diffraction data by the superposition of reciprocal lattices of the 3 domains (Fig. 3c), with three equivalent strain axes that are 120° apart. Crystals often break during the phase transition to release the elastic stress associated with the ferroelastic distortion and therefore we could not monitor the deviation of γ lattice angle from 120°.

Fig. 4b shows the large volume strain associated with the phase transition, defined as:

$$v_s(T) = \frac{V_{LT}(T)}{V_{HT}(T)} - 1 \quad (8)$$

where $V_{LT}(T)$ is the low-temperature phase volume at T and $V_{HT}(T)$ the high-temperature one, extrapolated at T. $v_s(T)$, normalized to the number of formula unit Z per unit cell, also exhibits thermal hysteresis curves concomitant with the symmetry-breaking ones. These data confirm that SB and SCO phenomena coincide, which results from their coupling as theoretically explained for $[Fe(ptz)_6](BF_4)_2$.[2a,3b]

Thermal quenching of the LShs phase. Fig. 3 shows the lattice parameters of the LShs phase, obtained on fast cooling to 80 K, with a $R\bar{3}$ lattice ($a_H = b_H$, $\alpha = \beta = 90°$ and $\gamma = 120°$). We notice a slight deviation from the thermal contraction of the lattice parameters extrapolated from the HShs phase. This partial volume strain ($v_{SCO} = -0.015(1)$) is then only due to the SCO of the Fe centres of (**1**) and is characteristic of the HShs → LShs conversion.[7d] During the phase transitions, the SB is monitored with the order parameter η, while the SCO is

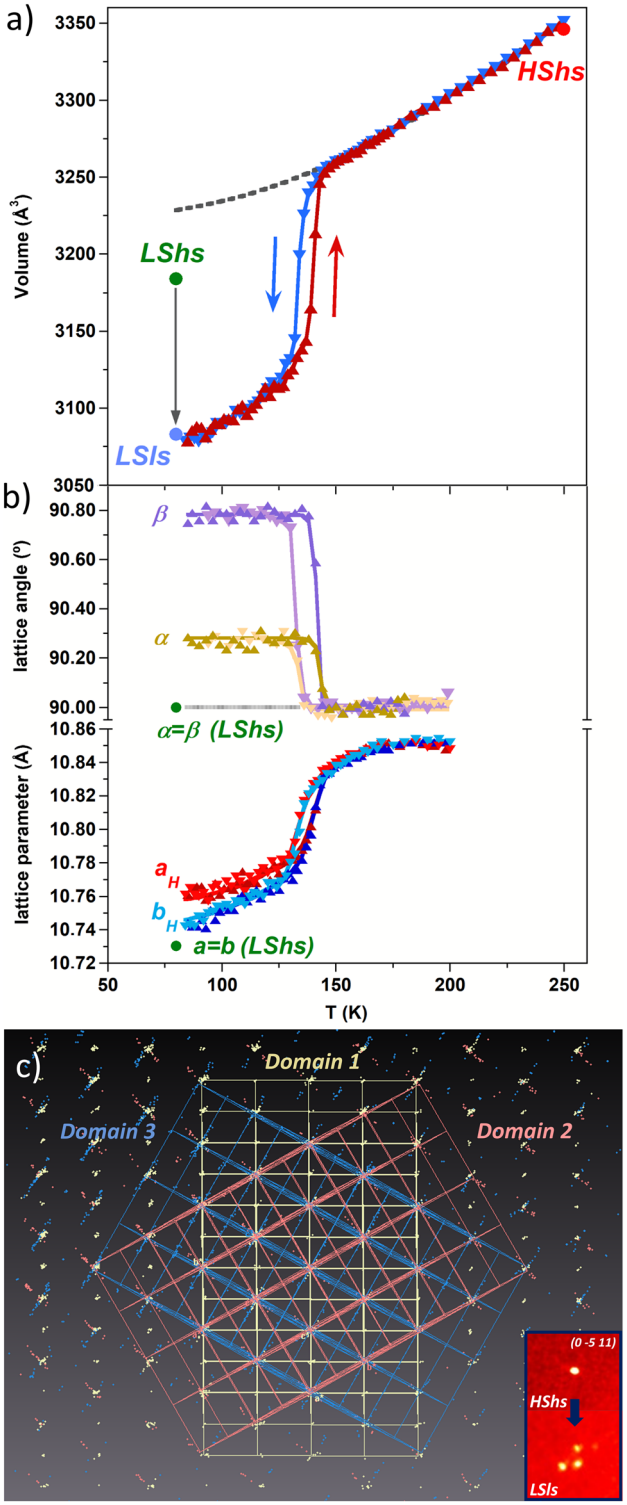

Fig. 3 Thermal dependence of the (pseudo) hexagonal cell volume (a) and lattice parameters a_H, b_H, α and β (b) between the HShs and LSIs phases. The parameters of the LShs phase are shown by the green dots. (c) In the LSIs phase, the X-ray diffraction signal is the superposition of the Bragg peaks from the 3 different ferroelastic domains that are 120° apart upon the $R\bar{3} \rightarrow P\bar{1}$ phase transition, which is also characterized by the peak splitting of Bragg peaks such as (0–5 11) shown in the inset.

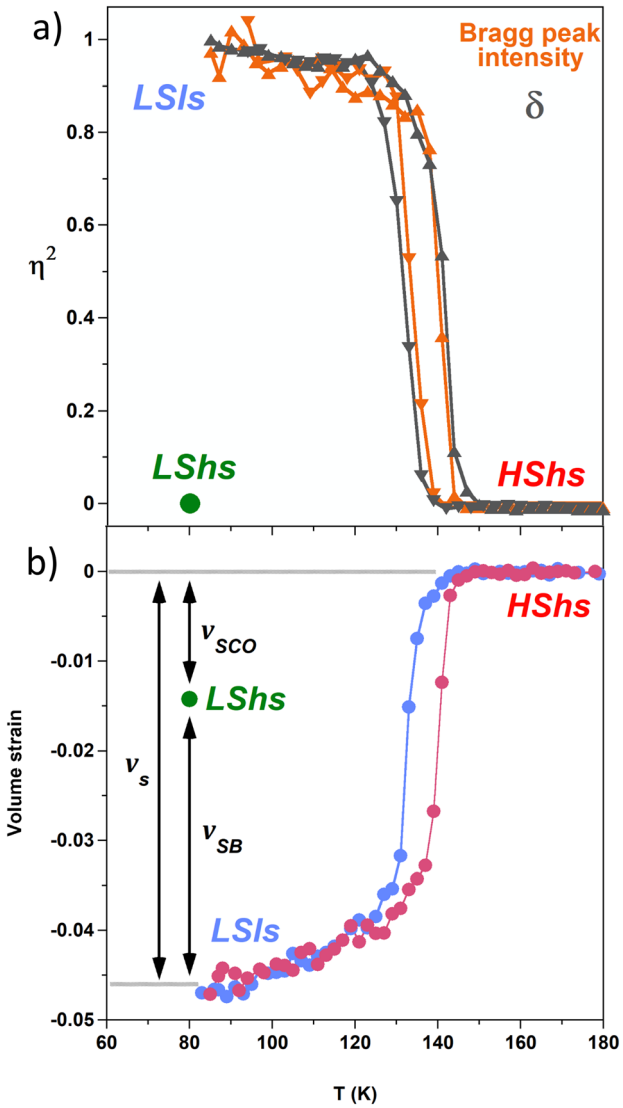

Fig. 4 (a) Thermal signatures of the $R\bar{3} \rightarrow P\bar{1}$ symmetry breaking monitored through the parameter δ probing the ferroelastic lattice distortions and through the intensity of the symmetry-breaking Bragg peaks. (b) Corresponding volume strain in the LSIs and LShs phases.

monitored through $q = \frac{N_{HS} - N_{LS}}{N_{HS} + N_{LS}}$ (N_{HS} and N_{LS} denote the number of sites in high or low spin states). The Landau analysis[3c] has shown that both SCO and SB couple, and therefore contribute to v_s:

$$v_s = -\frac{\left[\lambda_q\left(\frac{1-q}{2}\right) + \lambda_\eta \eta^2\right]}{C_s^0} = v_{SCO} + v_{SB} \quad (9)$$

For the $[Fe(ptz)_6](BF_4)_2$ it was found that v_s = −0.058(1), which includes both SCO and SB contributions.

Reorganisation of the molecular structures and packing. The reversible conversion between the different phases accessible upon the $R\bar{3} \rightarrow P\bar{1}$ ferroelastic phase transition is accompanied by a significant number of structural rearrangements at the intra- and inter-molecular levels,

involving both the cationic complexes and the tetrahedral BF_4^- counter-anions. The metallic centres of the complex, constituted by a mixture of iron(II) and ruthenium(II) ions in 0.65 : 0.35 percentage, are surrounded by six 1-propyl-1*H*-tetrazole ligands defining a slightly distorted octahedral [M^{II}-N_6] coordination environment around the metal M. Table 1 contains the average metal–nitrogen bond lengths and the deviation from the ideal octahedral geometry of the coordination sphere in the different phases, often used to characterise the spin state.[13] The average ⟨M–N⟩ bond length contraction between the HShs phase and the two high and low symmetry LS phases are very similar (0.102 Å and 0.101 Å, respectively). They are in good agreement with a complete spin transition of all the SCO-active Fe sites and clearly show the possibility of decoupling the $R\bar{3} \rightarrow P\bar{1}$ ferroelastic phase transition from the SCO. The experimental M^{II}–N values reported for the $[Ru_{0.35}Fe_{0.65}(ptz)_6](BF_4)_2$ in the HShs (2.128 Å) and the LSls phase (2.027 Å) are quite comparable to the expected values considering the values obtained for the pure Fe and Ru complexes:

$$d(M^{II}\text{–N})_{HShs} = \langle Fe^{II}\text{–N}\rangle_{HShs} \times 0.65 + \langle Ru^{II}\text{–N}\rangle_{hs} \times 0.35 = 2.134 \text{ Å and } d(M^{II}\text{–N})_{LSls} = \langle Fe^{II}\text{–N}\rangle_{LSls} \times 0.65 + \langle Ru^{II}\text{–N}\rangle_{ls} \times 0.35 = 2.021 \text{ Å}.$$

In the same way, for $[Fe(ptz)_6](BF_4)_2$,[2a] the volume strain due to the SCO between the HShs phase and the LShs phase, thermally quenched at 84 K is $\nu_{SCO} = -0.028(1)$, while the volume strain only due to the ferroelastic distortion between LShs phase and the LSls phase is $\nu_{SB} = -0.031(1)$.[2a] This is a nice illustration that the total volume strain ν_s associated with the HShs → LSls transition includes ν_{SB} and ν_{SCO} components as $\nu_s = -0.058 \simeq \nu_{SCO} + \nu_{SB}$. In the case of $[Ru_{0.35}Fe_{0.65}(ptz)_6](BF_4)_2$, we find $\nu_{SCO} = -0.015(1)$ and $\nu_{SB} = -0.032(1)$. ν_{SB} are similar for $[Ru_{0.35}Fe_{0.65}(ptz)_6](BF_4)_2$ and $[Fe(ptz)_6](BF_4)_2$ as both crystals exhibit similar ferroelastic distortion. However, ν_{SCO} in $[Ru_{0.35}Fe_{0.65}(ptz)_6](BF_4)_2$ is $\simeq\frac{2}{3}\nu_{SCO}$ of $[Fe(ptz)_6](BF_4)_2$, due to the chemical composition including only 2/3 of SCO-active Fe sites. Fig. 5a shows the molecular overlay of the cationic complex in the HShs, LShs, and LSls phases. Small changes are appreciable when the HShs and LShs phases are compared, which involve a subtle reorganisation of the core [MN_6] due to the spin state change, as can be seen from the average angular (Σ) and trigonal (Θ) distortion[13] in Table 1, and an order–disorder transition of the *n*-propyl groups.

It is important to emphasise that in both phases the 6 *n*-propyl groups of different monodentate ligands are symmetry-equivalent, by the rotoinversion $\bar{3}$ symmetry element located on the Fe, keeping therefore same *gauche* conformation. The dihedral angle changes from 59.76° in the HShs phase to 58.40° in the LShs phase. When the SB phase transition occurs, the *n*-propyl groups of the different ligands are no more equivalent due to the loss of the $\bar{3}$ symmetry. In the LSls phase, four crystallographically independent *n*-propyl groups retain the same conformational position, showing torsion angles that can vary between 55.97° and 58.60°, similar to those reported for the HShs and LShs phases.

A stronger rearrangement of the two-remaining *n*-propyl groups can be easily seen. From one side, the *n*-propyl group associated with the C2B–C3B–C4B fragment adopts a new *gauche* conformation after a rotation of 133.28° of the C4B carbon atom. On the other hand, a more significant change occurs in the fragment C2A–C3A–C4A, where an isomeric transition from *gauche*- to *anti*-conformation takes place. Fig. 5b shows the evolution of the supramolecular rearrangements with $\bar{3}$ and $\bar{1}$ symmetry elements in the HShs phase. In the LSls $P\bar{1}$ phase the $\bar{3}$ symmetry is lost and some $\bar{1}$ symmetry elements are kept in-between some cations complexes. These cation complexes interact with each other through numerous BF_4^- counter anions as shown in Fig. 6a. The number and strength of these intermolecular contacts depend on the spin state and the symmetry of (**1**) (Table 2). In the HShs phase, the counter-anions are located on 3-fold axis and display a static disorder between two specific positions (not shown). There are two different types of symmetry-equivalent intermolecular contacts below the Van der Waals radius. When the spin transition is induced without changing the symmetry, generating the LShs phase, the number of symmetry-equivalent intermolecular contacts significantly increases due to the lattice contraction, favouring the formation of a set of particularly very short N···F contacts [d(N4···F2) = 2.890 Å]. In addition, the static disorder of the BF_4^- anions disappears, locking the anionic moieties in one of the preferential positions displayed in the HShs phase. The LSls phase also shows a higher number of intermolecular contacts when compared with the HShs phase, but in less extension than the LShs phase does. The $R\bar{3} \rightarrow P\bar{1}$ ferroelastic phase transition is accompanied by an essential displacement of the BF_4^- anions in the crystal lattice, significantly impacting the possible supramolecular contacts that can rise between the cationic complex and the counter-anions.

Another characteristic of the symmetry breaking is shown in Fig. 6b. In the $R\bar{3}$ phase, the BF_4^- tetrahedra are located on 3-fold Wyckoff positions, with one of the F atoms on the 3-fold axis and pointing up or down along the *c* axis. In the LSls phase, the 3-fold axis is lost, and the tetrahedra can point in any direction. The new disposition of the BF_4^- plus

Table 1 Average M^{II}–N bond lengths and distortion parameters Σ and Θ of the $M^{II}N_6$ octahedra in the HShs, LShs and LSls phases, with $\Sigma = \sum_{i=1}^{12} |90 - \Phi_i|$ and $\Theta = \sum_{i=1}^{24} (|60 - \theta_i|)$ as defined in ref. 13

	LSls (80 K)	LShs (80 K)	HShs (250 K)
⟨M^{II}–N⟩ (Å)	2.027	2.026	2.128
Σ (°)	10.3	6.9	4.1
Θ (°)	15.0	7.9	4.7

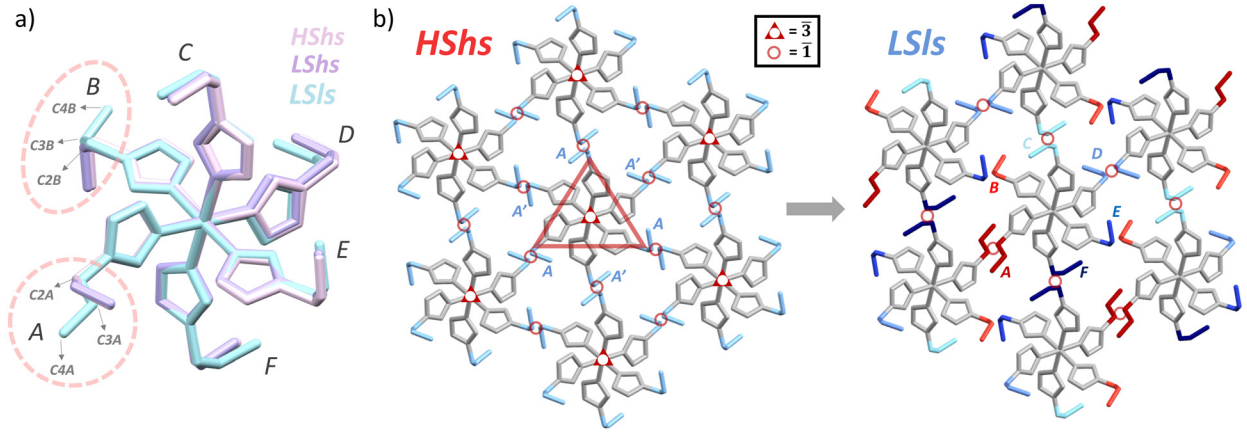

Fig. 5 a) Minimised overlay of the cationic complex in the HShs (pink), LShs (purple) and LSls (green) phases showing the conformational changes of *n*-propyl groups (C2A–C3A–C4A and C2B–C3B–C4B) in circled areas. Disorder of *n*-propyl group in the HShs phase is omitted for clarity. b) Symmetry-breaking associated with rearrangement of propyl groups, viewed along the *c* axis of the (pseudo) rhombohedral lattice. In the HShs and LShs states, the cations are located on $\bar{3}$ symmetry with equivalent A–B–C–D–E–F *n*-propyl groups. The cations are related by 3-fold and inversion symmetry. In the LSls phase the 3-fold axis are lost and some $\bar{1}$ symmetry elements are kept in the $P\bar{1}$ lattice.

the special rearrangement of the *n*-propyl groups are some of the identity signatures of the ferroelastic phase transition. The molecular rearrangement is also associated with a shear strain, shown in Fig. 6b, with opposite motions of the cation layers in the (*a*, *b*) plane (grey arrows) responsible for the deviation of the lattice angles α and β from 90°.

The neutral layers of complexes are stacked along the *c* direction in the HShs and LShs phases through very weak intermolecular contacts between the *n*-propyl groups pointing to the interlayer space. The distance between the layers is 11.007 Å and 10.641 Å for the HShs and LShs phases, respectively. The same stacking can be detected in the LSls phase, showing an interlayer distance slightly smaller than that for the LShs phase (10.224 Å). In addition, the molecular packing clearly shows the shear strain with the deviation of the angle β from 90° in the $P\bar{1}$ phase, as it is illustrated in the Fig. 6b.

Origin of the metastable LShs phase. All these experimental data provide key information on the change of spin state and crystalline structures between the HShs, LShs, and LSls phases. In SCO materials, structural trapping of HShs state at low temperatures was reported in many

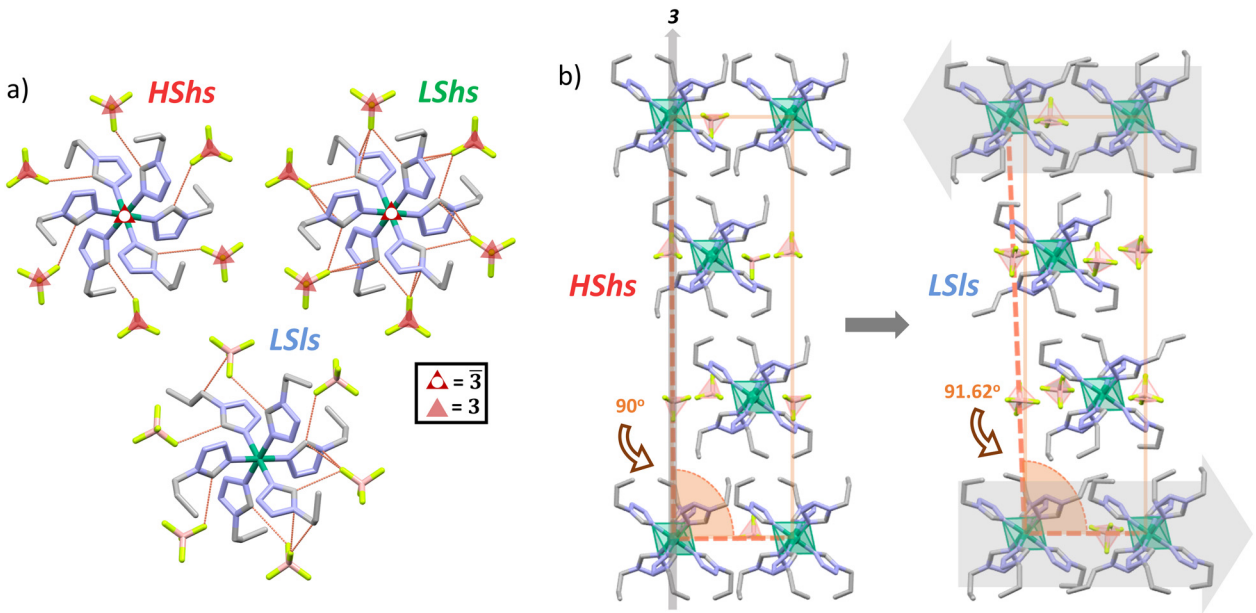

Fig. 6 a) Intermolecular contacts between the cationic complex located on $\bar{3}$ symmetry and BF_4^- counter-anions located on 3-fold symmetry axis in the HShs and LShs. In the LSls the inter-molecular contacts are no more symmetry-equivalent. b) Ferroelastic distortion upon the $R\bar{3} \rightarrow P\bar{1}$ transformation of the lattice viewed along the *b* axis of the pseudo-rhombohedral lattice, with a shear strain shown by the grey arrows. Hydrogen atoms and possible disorder of both *n*-propyl groups and BF_4^- counter-anions are omitted for clarity.

Table 2 Intermolecular contacts for the HShs, LShs and LSls phases

Inter. contact	HShs (250 K)	Inter. contact	LShs (80 K)	Inter. contact	LSls (80 K)
C1–F2	3.156 Å	C1–F2	3.128 Å	C1A–F7	3.108 Å
C3′–F1	3.028 Å	C1–F2	3.170 Å	C1B–F5	3.095 Å
		N4–F2	2.890 Å	C1C–F1	3.169 Å
				C1D–F4	3.130 Å
				C1E–F6	3.164 Å
				C1F–F4	3.113 Å
				C1F–F2	3.125 Å
				C2A–F8	3.112 Å
				C2D–F3	3.116 Å
				N4D–F3	3.004 Å
				N4F–F4	2.997 Å

systems.[1e,7d,14] The key feature related to such metastable HS state is the energy barrier between the HS and LS states and the thermally activated relaxation. However, this can't explain the occurrence of a metastable LShs phase observed in $[Ru_{0.35}Fe_{0.65}(ptz)_6](BF_4)_2$ or in the pure $[Fe(ptz)_6](BF_4)_2$ materials. To understand the metastable LShs state, we need to discuss in more details Collet's approach of the Landau theory of phase transition applied to SCO materials exhibiting symmetry breaking.[2a,3b,c] As explained in the case of $[Fe(ptz)_6](BF_4)_2$, which exhibits similar SCO and SB, the simplest symmetry-adapted Landau potential to describe simultaneously SCO, measured through the order parameter q, and symmetry breaking η, takes the following form:

$$G(q,\eta) = \frac{1}{2}a\eta^2 + \frac{1}{3}b\eta^3 + \frac{1}{4}c\eta^4 + Aq + \frac{1}{2}Bq^2 + \frac{1}{4}Cq^4 + \frac{1}{2}{C_s}^0{v_s}^2 + \lambda_\eta v_s\eta^2 + \lambda_q v_s\left(\frac{1-q}{2}\right) \quad (10)$$

where the η^2, η^3, η^4 terms describe the usual Landau SB potential for $R\bar{3} \rightarrow P\bar{1}$ ferroelastic transition, with $a = a_0(T - T_{SB})$ and $c > 0$ for stability.[12d] The coefficient a changes sign at the symmetry-breaking temperature T_{SB}, which stabilizes $\eta = 0$ above T_{SB} and $\eta \neq 0$ below. Similarly, the q, q^2, q^4 terms describe the SCO as A changes linearly with T.[15] In this model, a key point is to consider the elastic contributions to the potential: the elastic energy $\frac{1}{2}{C_s}^0{v_s}^2$ related to elastic constant ${C_s}^0$, as well as the elastic coupling to v_s of i) the ferroelastic distortion $(\lambda_\eta v_s\eta^2)$ and ii) the SCO where $\lambda_q v_s\left(\frac{1-q}{2}\right)$ both taken as reference in HS state ($q = 1$). Collet *et al.* have shown that the equilibrium volume strain includes contributions from both SCO and SB[2a,3b,c] and scales as: $v_s = v_{SCO} + v_{SB}$. Substituting in eqn (10) v_s given in eqn (9) results in the renormalized thermodynamic potential:

$$G(q,\eta) = \frac{1}{2}a\eta^2 + \frac{1}{3}b\eta^3 + \frac{1}{4}c\eta^4 + Aq + \frac{1}{2}Bq^2 + \frac{1}{4}Cq^4 + Dq\eta^2 \quad (11)$$

where the SB–SCO coupling term $Dq\eta^2$ appears, with $D > 0$ which stabilizes HShs or LSls phases.

The 2D contour plots of $G(q, \eta)$ in Fig. 7 show how the stability of the HShs ($q = 1$, $\eta = 0$) or LSls phase ($q = -1$, $\eta \neq 0$) changes with temperature at equilibrium when both SB and SCO degrees of freedom. This is due to the considerable volume strain v_S, including v_{SCO} and v_{SB}, which stabilises either the HShs or the LSls phase. Under pressure, $[Fe(ptz)_6](BF_4)_2$ exhibits sequential SB and SCO with an intermediate HSls phase.[4c,e] Consequently, the volume strain also evolves sequentially with a first contraction (v_{SB}) at high temperature during the SB phase transition and another one (v_{SCO}) at a lower temperature due to SCO. v_{SCO} and v_{SB} have similar amplitudes and at ambient pressure $v_s \simeq v_{SCO} + v_{SB}$.[2a]

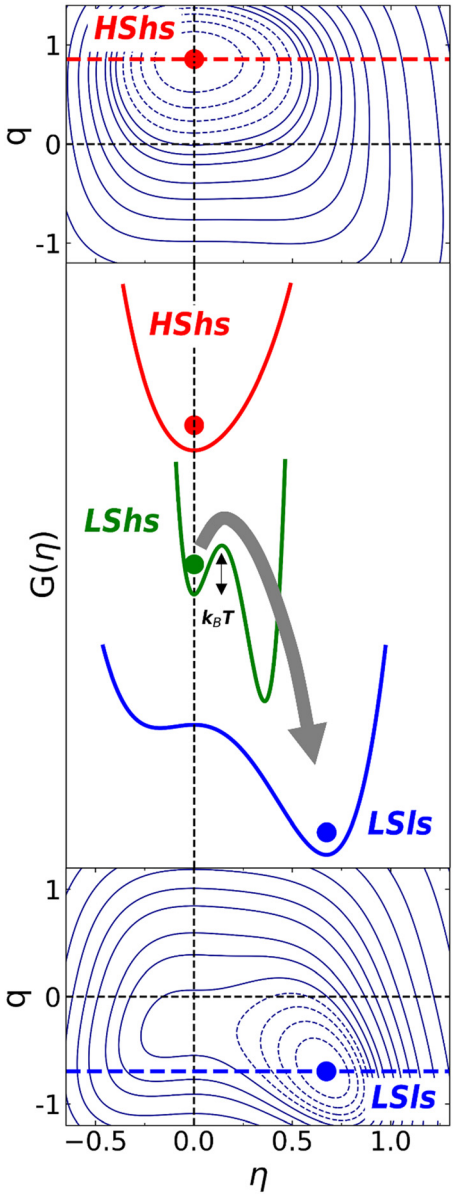

Fig. 7 2D contour map of the thermodynamic potential $G(q, \eta)$ in eqn (11) along the spin state (q) and symmetry breaking (η) degrees of freedom. At high temperature (top) the HShs state corresponding to ($q \simeq 1$, $\eta = 0$) is stable. At low temperature (bottom) the LSls state ($q \simeq -1$, $\eta \neq 0$) is stable. The central panel shows corresponding cuts along the symmetry-breaking axis for the HShs (red) and LSls (blue) phases. In the case of flash cooling, allowing SCO but not SB, the reduced volume strain can generate a metastable LShs state ($q \simeq -1$, $\eta = 0$).

However, on changing temperature from HShs to LSls, the LShs phase does not form at intermediate temperature with this potential. To explain the appearance of the LShs metastable phase, let's consider for simplicity the symmetry-breaking part of the Landau-type expansion of the Gibbs energy describing the $R\bar{3} \rightarrow P\bar{1}$ ferroelastic phase transition:[12b,c,16]

$$G(\eta) = \frac{1}{2}a'\eta^2 + \frac{1}{3}b\eta^3 + \frac{1}{4}c\eta^4 \quad (12)$$

The renormalisation of the coefficient $a' = a + 2\lambda_\eta v_s$ includes the elastic coupling of the symmetry breaking to the volume strain ($v_s < 0$ and $\lambda_\eta > 0$). Above T_{SB} in the HShs phase a' (HShs) > 0 (since $a > 0$ and $v_s = 0$). Therefore, the potential (11) along η shows a high symmetry equilibrium phase ($\eta = 0$) corresponding to the $R\bar{3}$ lattice (red curve in Fig. 7). The LSls phase ($a < 0$) v_s includes SCO and SB components ($v_{SCO} + v_{SB} = v_s < 0$) and a'(LSls) $= a + 2\lambda_\eta v_s < 0$. The $\frac{1}{2}(a + 2\lambda_\eta v_s)\eta^2$ term stabilises the low symmetry $P\bar{1}$ lattice with a minimum for $\eta \neq 0$ (blue curve in Fig. 7). On fast cooling, SCO occurs, due to rapid equilibration of the spin state degrees of freedom; while slower long-range lattice ordering and propagation of shear strains preclude the emergence of SB. The volume strains on fast cooling (v_{FC}) towards the LShs state are then reduced to the sole contribution of the SCO: $v_{FC} \simeq v_{SCO}$. This situation, which is intermediate between the HShs and LSls cases, can generate a metastable LShs state as the elastic coupling gain of the symmetry-breaking is reduced to v_{FC}. The $\frac{1}{2}(a + 2\lambda_\eta v_{FC})\eta^2$ term with reduced amplitude stabilises less the low symmetry $P\bar{1}$ lattice ($\eta \neq 0$) and generates a metastable LShs state ($\eta = 0$), as shown by the green potential curve in Fig. 7. If the energy barrier is of the order of the thermal energy (k_BT), the system may thermally relax towards the stable LSls phase, which will be even more stabilised by an additional symmetry-breaking component of the volume strain.

Conclusion

The present study shows that for understanding thermal-equilibrium properties and the emergence of metastable phases in the $[Ru_{0.35}Fe_{0.65}(ptz)_6](BF_4)_2$ material, derivate from the original $[Fe(ptz)_6](BF_4)_2$ system, it is essential to consider SCO and SB phenomena and their coupling to the volume strain. The critical point is that both SCO and SB contribute to the volume strain, almost equally. At thermal equilibrium on slow cooling, the spin state and symmetry-breaking degrees of freedom have time to equilibrate, which induces a large volume strain that stabilises the low-spin low-symmetry phase. On flash cooling, the SCO occurs, but long-range symmetry breaking doesn't have time to set up. The reduced volume strain, limited to the contribution of the SCO, is responsible for the appearance of a metastable LShs phase. We are therefore convinced that such analysis can be expanded to other SCO compounds, and more generally to other classes of materials exhibiting a coupled change of electronic state and symmetry.

Author contributions

Francisco Javier Valverde-Muñoz: methodology, data curation, formal analysis, writing – original draft; Ricardo Guillermo Torres Ramírez: conceptualization, data curation; Abhilash Ulhe: data curation, formal analysis; Elzbieta Trzop: supervision, methodology, data curation, formal analysis, review & editing; Mousumi Dutta and Chinmoy Das: syntheses and growth of the single crystals $[Ru_{0.35}Fe_{0.65}(ptz)_6](BF_4)_2$, and manuscript editing; Pradip Chakraborty: resources, review & editing; Eric Collet: funding acquisition, data curation, investigation, conceptualization, supervision, writing – original draft, review & editing. All authors critically reviewed and revised the manuscript draft and approved the final version for submission.

Conflicts of interest

There are no conflicts to declare.

Acknowledgements

This work was supported in part by Agence Nationale de la Recherche for financial support under the grant ANR-19-CE30-0004 ELECTROPHONE, ANR-19-CE07-0027 SMAC. EC thanks the University Rennes and the Fondation Rennes 1 for funding. F. J. V.-M. acknowledges the support of the European Social Fund (ESF) and Generalitat Valenciana for his postdoctoral fellowship (APOSTD/2021/359). The authors thank Région Bretagne, Ille-Et-Vilaine Department, French Ministry of Research, Rennes Métropole, CNRS, European Union for financial support (CPER Project Mat&Trans 2021-2027). PC acknowledges financial support from SERB (Grant No. ECR/2018/000923) and Indian Institute of Technology Kharagpur (Grant no. IIT/SRIC/CY/ENE/2018-19/194). MD and CD acknowledge Indian Institute of Technology Kharagpur for research fellowship.

References

1 (*a*) H. Tokoro and S. Ohkoshi, *Bull. Chem. Soc. Jpn.*, 2015, **88**, 227; (*b*) Y. S. Meng, O. Sato and T. Liu, *Angew. Chem., Int. Ed.*, 2018, **57**, 12216; (*c*) E. Pardo, C. Train, H. Liu, L.-M. Chamoreau, B. Dkhil, K. Boubekeur, F. Lloret, K. Nakatani, H. Tokoro, S. Ohkoshi and M. Verdaguer, *Angew. Chem.*, 2012, **124**, 8481; (*d*) D. Aguila, Y. Prado, E. S. Koumousi, C. Mathoniere and R. Clerac, *Chem. Soc. Rev.*, 2016, **45**, 203; (*e*) M. A. Halcrow, *Spin-crossover materials: properties and applications*, John Wiley & Sons, Ltd, Chichester, 2013; (*f*) P. Gutlich, A. Hauser and H. Spiering, *Angew. Chem., Int. Ed. Engl.*, 1994, **33**, 2024; (*g*) A. Bousseksou, G. Molnar, L. Salmon and W. Nicolazzi, *Chem. Soc. Rev.*, 2011, **40**, 3313; (*h*) G. Molnár, M. Mikolasek, K. Ridier, A. Fahs, W. Nicolazzi and A. Bousseksou, *Ann. Phys.*, 2019, **531**, 1900076; (*i*) S.

Koshihara, T. Ishikawa, Y. Okimoto, K. Onda, R. Fukaya, M. Hada, Y. Hayashi, S. Ishihara and T. Luty, *Phys. Rep.*, 2022, **942**, 1; (*j*) T. Ishikawa, S. A. Hayes, S. Keskin, G. Corthey, M. Hada, K. Pichugin, A. Marx, J. Hirscht, K. Shionuma, K. Onda, Y. Okimoto, S.-Y. Koshihara, T. Yamamoto, H. Cui, M. Nomura, Y. Oshima, M. Abdel-Jawad, R. Kato and R. J. D. Miller, *Science*, 2015, **350**, 1501; (*k*) M. Chollet, L. Guerin, N. Uchida, S. Fukaya, H. Shimoda, T. Ishikawa, K. Matsuda, T. Hasegawa, A. Ota, H. Yamochi, G. Saito, R. Tazaki, S.-I. Adachi and S.-Y. Koshihara, *Science*, 2005, **307**, 86; (*l*) L. Guerin, E. Collet, M. H. Lemee-Cailleau, M. Buron-Le Cointe, H. Cailleau, A. Plech, M. Wulff, S. Y. Koshihara and T. Luty, *Chem. Phys.*, 2004, **299**, 163.

2 (*a*) E. Collet, G. Azzolina, J. Jeftić and M.-H. Lemée-Cailleau, *Adv. Phys.: X*, 2023, **8**, 2161936; (*b*) V. B. Jakobsen, E. Trzop, E. Dobbelaar, L. C. Gavin, S. Chikara, X. Ding, M. Lee, K. Esien, H. Müller-Bunz, S. Felton, E. Collet, M. A. Carpenter, V. S. Zapf and G. G. Morgan, *J. Am. Chem. Soc.*, 2022, **144**, 195; (*c*) A. Slimani and K. Boukheddaden, *J. Appl. Phys.*, 2021, **129**, 173901; (*d*) J. Cruddas and B. J. Powell, *Inorg. Chem. Front.*, 2020, **7**, 4424; (*e*) G. Félix, M. Mikolasek, H. J. Shepherd, J. Long, J. Larionova, Y. Guari, J.-P. Itié, A. I. Chumakov, W. Nicolazzi, G. Molnár and A. Bousseksou, *Eur. J. Inorg. Chem.*, 2018, **2018**, 443; (*f*) C. Enachescu and W. Nicolazzi, *C. R. Chim.*, 2018, **21**, 1179; (*g*) W. Nicolazzi and A. Bousseksou, *C. R. Chim.*, 2018, **21**, 1060; (*h*) H. Yamochi and S.-Y. Koshihara, *Sci. Technol. Adv. Mater.*, 2009, **10**, 024305.

3 (*a*) G. Azzolina, R. Bertoni and E. Collet, *J. Appl. Phys.*, 2021, **129**, 085106; (*b*) E. Collet and G. Azzolina, *Phys. Rev. Mater.*, 2021, **5**, 044401; (*c*) G. Azzolina, R. Bertoni, C. Ecolivet, H. Tokoro, S. Ohkoshi and E. Collet, *Phys. Rev. B*, 2020, **102**, 134104; (*d*) M. Shatruk, H. Phan, B. A. Chrisostomo and A. Suleimenova, *Coord. Chem. Rev.*, 2015, **289–290**, 62; (*e*) D. Paliwoda, L. Vendier, W. Nicolazzi, G. Molnár and A. Bousseksou, *Inorg. Chem.*, 2022, 15991; (*f*) R. Li, G. Levchenko, F. J. Valverde-Muñoz, A. B. Gaspar, V. V. Ivashko, Q. Li, B. Liu, M. Yuan, H. Fylymonov and J. A. Real, *Inorg. Chem.*, 2021, **60**, 16016; (*g*) V. B. Jakobsen, E. Trzop, L. C. Gavin, E. Dobbelaar, S. Chikara, X. Ding, K. Esien, H. Müller-Bunz, S. Felton, V. S. Zapf, E. Collet, M. A. Carpenter and G. G. Morgan, *Angew. Chem., Int. Ed.*, 2020, **59**, 13305; (*h*) V. B. Jakobsen, S. Chikara, J.-X. Yu, E. Dobbelaar, C. T. Kelly, X. Ding, F. Weickert, E. Trzop, E. Collet, H.-P. Cheng, G. G. Morgan and V. S. Zapf, *Inorg. Chem.*, 2021, 6167; (*i*) M. Nihei, Y. Okamoto, Y. Sekine, N. Hoshino, T. Shiga, I. P.-C. Liu and H. Oshio, *Angew. Chem., Int. Ed.*, 2012, **51**, 6361.

4 (*a*) J. Kusz, M. Zubko, R. B. Neder and P. Gutlich, *Acta Crystallogr., Sect. B: Struct. Sci.*, 2012, **68**, 40; (*b*) S. Lakhloufi, P. Guionneau, M. H. Lemée-Cailleau, P. Rosa and J. F. Létard, *Phys. Rev. B: Condens. Matter Mater. Phys.*, 2010, **82**, 132104; (*c*) M.-H. Lemée-Cailleau, C. Ecolivet, B. Ouladdiaf, F. Moussa and J.-F. Létard, *Phys. B*, 2009, **404**, 379; (*d*) A. Goujon, F. Varret, K. Boukheddaden, C. Chong, J. Jeftić, Y. Garcia, A. D. Naik, J. C. Ameline and E. Collet, *Inorg. Chim. Acta*, 2008, **361**, 4055; (*e*) M. H. Lemée-Cailleau, C. Ecolivet, B. Ouladdiaf, F. Moussa, J. Jeftic and J. F. Létard, *J. Magn. Magn. Mater.*, 2007, **310**, 1792; (*f*) J. Jeftić, H. Romstedt and A. Hauser, *J. Phys. Chem. Solids*, 1996, **57**, 1743; (*g*) A. Hauser, *Chem. Phys. Lett.*, 1992, **192**, 65; (*h*) L. Wiehl, H. Spiering, P. Gutlich and K. Knorr, *J. Appl. Crystallogr.*, 1990, **23**, 151; (*i*) P. Gutlich and H. A. Goodwin, *Spin Crossover in Transition Metal Compounds I*, 2004, vol. 233, p. 1.

5 (*a*) L. Wiehl, *Acta Crystallogr., Sect. B: Struct. Sci.*, 1993, **49**, 289; (*b*) P. Gutlich, Y. Garcia and H. A. Goodwin, *Chem. Soc. Rev.*, 2000, **29**, 419; (*c*) A. Marino, P. Chakraborty, M. Servol, M. Lorenc, E. Collet and A. Hauser, *Angew. Chem., Int. Ed.*, 2014, **53**, 3863; (*d*) A. Hauser, *J. Chem. Phys.*, 1991, **94**, 2741; (*e*) J. Jeftić and A. Hauser, *J. Phys. Chem. B*, 1997, **101**, 10262.

6 G. Privault, J.-Y. Mevellec, M. Lorenc, B. Humbert, E. Janod, N. Daro, G. Chastanet, A. Subedi and E. Collet, *Cryst. Growth Des.*, 2022, **22**, 5100.

7 (*a*) A. Ozarowski and B. R. McGarvey, *Inorg. Chem.*, 1989, **28**, 2262; (*b*) J. Jung, F. Bruchhäuser, R. Feile, H. Spiering and P. Gütlich, *Z. Phys. B: Condens. Matter*, 1996, **100**, 517; (*c*) J. Jung, G. Schmitt, L. Wiehl, A. Hauser, K. Knorr, H. Spiering and P. Gütlich, *Z. Phys. B: Condens. Matter*, 1996, **100**, 523; (*d*) P. Chakraborty, M. Sy, H. Fourati, T. Delgado, M. Dutta, C. Das, C. Besnard, A. Hauser, C. Enachescu and K. Boukheddaden, *Phys. Chem. Chem. Phys.*, 2022, **24**, 982.

8 G. Sheldrick, *Acta Crystallogr., Sect. A: Found. Adv.*, 2015, **71**, 3.

9 G. Sheldrick, *Acta Crystallogr., Sect. C: Struct. Chem.*, 2015, **71**, 3.

10 O. V. Dolomanov, L. J. Bourhis, R. J. Gildea, J. A. K. Howard and H. Puschmann, *J. Appl. Crystallogr.*, 2009, **42**, 339.

11 H. T. Stokes and D. M. Hatch, *Isotropy Subgroups of the 230 Crystallographic Space Groups*, 1988.

12 (*a*) E. K. H. Salje, *Annu. Rev. Mater. Res.*, 2012, **42**, 265; (*b*) M. A. Carpenter, E. K. H. Salje and A. Graeme-Barber, *Eur. J. Mineral.*, 1998, **10**, 621; (*c*) M. A. Carpenter and E. K. Salje, *Eur. J. Mineral.*, 1998, **10**, 693; (*d*) E. K. Salje, *Phase Transitions in Ferroelastic and Co-elastic Crystals*, Cambridge University Press, Cambridge, 1991.

13 E. Collet and P. Guionneau, *C. R. Chim.*, 2018, **21**, 1133.

14 (*a*) G. Molnár, S. Rat, L. Salmon, W. Nicolazzi and A. Bousseksou, *Adv. Mater.*, 2018, **30**, 1703862; (*b*) A. Hauser, *Top. Curr. Chem.*, 2004, **234**, 155; (*c*) M. Marchivie, P. Guionneau, J. F. Letard, D. Chasseau and J. A. K. Howard, *J. Phys. Chem. Solids*, 2004, **65**, 17.

15 D. Chernyshov, H.-B. Bürgi, M. Hostettler and K. W. Törnroos, *Phys. Rev. B: Condens. Matter Mater. Phys.*, 2004, **70**, 094116.

16 E. K. Salje and M. A. Carpenter, *J. Phys.: Condens. Matter*, 2011, **23**, 462202.